Piecewise-diffeomorphic image registration: Application to the motion estimation between 3D CT lung images with sliding conditions

Laurent Risser [a,*], François-Xavier Vialard [b], Habib Y. Baluwala [a], Julia A. Schnabel [a]

[a] Institute of Biomedical Engineering, Department of Engineering Science, University of Oxford, UK
[b] CEREMADE, Université de Paris-Dauphine, France

ABSTRACT

In this paper, we propose a new strategy for modelling sliding conditions when registering 3D images in a piecewise-diffeomorphic framework. More specifically, our main contribution is the development of a mathematical formalism to perform *Large Deformation Diffeomorphic Metric Mapping* registration with sliding conditions. We also show how to adapt this formalism to the *LogDemons* diffeomorphic registration framework. We finally show how to apply this strategy to estimate the respiratory motion between 3D CT pulmonary images. Quantitative tests are performed on 2D and 3D synthetic images, as well as on real 3D lung images from the MICCAI EMPIRE10 challenge. Results show that our strategy estimates accurate mappings of entire 3D thoracic image volumes that exhibit a sliding motion, as opposed to conventional registration methods which are not capable of capturing discontinuous deformations at the thoracic cage boundary. They also show that although the deformations are not smooth across the location of sliding conditions, they are almost always invertible in the whole image domain. This would be helpful for radiotherapy planning and delivery.

Crown Copyright © 2012 Published by Elsevier B.V. All rights reserved.

1. Introduction

Until recently, the main efforts to estimate the respiratory motion in lung imaging focused on image registration techniques based on B-splines (Mattes et al., 2003; McClelland et al., 2006), thin-plate splines (Coselmon et al., 2004; Li et al., 2003), hybrid feature- and intensity-based registration (Stewart et al., 2004), optical flow or diffusion (demons) type methods (Werner et al., 2010) with a spatially homogeneous regularisation of the deformations. A review of these techniques is given in (Sluimer et al., 2006). The MICCAI Evaluation of Methods for Pulmonary Image Registration 2010 (EMPIRE10) challenge (Murphy et al., 2011) allowed the comparison of state-of-the art algorithms for this purpose using a common dataset. None of the above mentioned methods is however designed to capture non-smooth, discontinuous sliding motion due to organ slippage adequately. Slippage between the lungs and surrounding structures is illustrated in Fig. 1, where we show the displacement of a vessel within the lungs, relative to two ribs. Sliding motion of the lungs against the chest wall naturally takes place across the pleura during breathing. The pleural cavity is a body cavity that surrounds the lungs and allows the pleurae to slide effortlessly against each other during ventilation. For this reason, standard methods, which do not explicitly model

sliding conditions, typically register only the lungs extracted from the background. For instance, the most successful methods of (Murphy et al., 2011) first affinely register the lung masks before performing a non-rigid registration of the masked lung CT images. Moreover, due to the sparse distribution of features within the lungs, a large amount of regularisation is required to properly register the lungs. This obviously leads to the estimation of non-natural deformations in the thoracic cage's neighbourhood, in particular, in the ribs and the spine, which exhibit a locally rigid motion. For a simultaneous registration of the lungs and their surroundings, models taking into account more information about the thoracic physiology, in particular sliding conditions, are consequently required. Clinical applications would benefit from incorporating sliding conditions when registering lung images, for instance in radiotherapy planning or in image guided surgery.

A recent approach to biomechanical patient-specific respiratory motion modelling is described in (Werner et al., 2009). This method is however computationally too complex to be used for automated image registration tasks. Several approaches for direction-dependent regularisation in diffusion- or spline-based registration frameworks were also recently introduced (Wu et al., 2008; Ruan et al., 2009; Schmidt-Richberg et al., 2012; Yin et al., 2010; Pace et al., 2011; Delmon et al., 2011; Vandemeulebroucke et al., 2012) for modelling sliding conditions. In particular (Wu et al., 2008; Vandemeulebroucke et al., 2012) use masked spline deformations and (Delmon et al., 2011) uses an additional spline

* Corresponding author.
  E-mail address: laurent.risser@gmail.com (L. Risser).

they can move in real applications. This is the case in our application where the regions can be the thoracic cage, which smoothly moves during the respiratory motion, and the rest of the image. In Section 4, we then show how to apply these algorithms to estimate the respiratory motion from image pairs exhibiting sliding motion. This is done by decomposing the registration into three steps: (1) We first align the thoracic cage boundaries without sliding motion modelling, (2) we then register the structures inside and outside the thoracic cage independently with sliding motion modelling, and (3) we perform a final refinement registration step without sliding motion modelling. Deformations computed at each step are composed, so the strategy of Section 4 can be seen as close to those of (Arsigny et al., 2009; Bruveris et al., 2012; Sommer et al., 2011b; Sommer et al., 2011a). Results and discussions are finally presented in Sections 5 and 6, respectively.

2. Piecewise-diffeomorphic LDDMM registration

2.1. LDDMM framework

In this subsection, we introduce the standard LDDMM registration algorithm (Beg et al., 2005). Let I_S be a source (moving) image registered to a target (fixed) image I_T in the domain $\Omega \subset \mathbb{R}^n$. These images are registered through the time-dependent diffeomorphic transformation $\phi:t \in [0,1] \mapsto \phi_t$, which is defined by the flow of a time dependent velocity field $\mathbf{v}:t \in [0,1] \mapsto \mathbf{v}_t$ using $\frac{\partial}{\partial t}\phi_t = \mathbf{v}_t$ (ϕ_t), $t \in [0,1]$, where $\phi_0 = \mathbf{Id}$. We introduce the notation $\phi_{s,t} \doteq \phi_t \circ \phi_s^{-1}$, the diffeomorphic transformation, so that $I \circ \phi_{s,t}^{-1}$ is I transported from time s to time t by ϕ. We also use $\phi_t \doteq \phi_{0,t}$. Note that the field $\mathbf{v}_t$ is defined on Ω and vanishes at the boundary, so ϕ is a diffeomorphism of Ω. The registration problem of (Beg et al., 2005) consists of estimating the velocity field $\mathbf{v}$ which minimises

$$E(\mathbf{v}) = \int_0^1 \frac{1}{2}\|\mathbf{v}_t\|_V^2 dt + \frac{1}{2}\|I_S \circ \phi_1^{-1} - I_T\|_{L^2}^2. \tag{1}$$

The first term measures the deformation amplitude and smoothness, and the second term measures the sum of squared differences (SSD) between the deformed source image $I_S \circ \phi_1^{-1}$ and I_T. The time-dependent velocity field $\mathbf{v}$ is assumed to lie in $L^2([0,1],V)$, where $[0,1]$ represents the time and the Hilbert space V is a Reproducing Kernel Hilbert Space (RKHS) of vector fields that can be continuously embedded in $C^1(\Omega,\mathbb{R}^n)$. More specifically, there exists a constant C_V such that

$$\|\mathbf{v}_t\|_{1,\infty} \leqslant C_V\|\mathbf{v}_t\|_V, \tag{2}$$

where $\mathbf{v}_t \in V$, and $\|\mathbf{v}_t\|_{1,\infty}$ refers to the L^∞ norm of $\mathbf{v}_t$ gradients. The condition in Eq. (2) ensures that the variational problem is well-posed, *i.e.* that there exists a minimiser and that the functional is differentiable for sufficiently smooth images. Gradient-based methods can then be applied to minimise Eq. (1). At time t, the norm can be computed by $\|\mathbf{v}_t\|_V^2 = <\mathcal{F}(\mathbf{v}_t)\mathcal{F}(K)^{-1}, \mathcal{F}(\mathbf{v}_t)>_{L^2}$, where $\mathcal{F}(\cdot)$ represents the Fourier transform and $<\cdot,\cdot>_{L^2}$ is the L^2 inner product. Although a wide family of kernels can be associated with V, most approaches use a simple Gaussian kernel K. The minimisation of the variational problem of Eq. (1) is performed using a steepest gradient descent approach (Beg et al., 2005). We denote $I_t^S = I_S \circ \phi_t^{-1}$, $I_t^T = I_T \circ \phi_{1,t}^{-1}$ and $\mathrm{Det}\mathrm{J}_{\phi_{t,1}}$ the determinant of Jacobian of $\phi_{t,1}$ at time t. At each iteration, the energy gradient $\mathbf{\nabla_v}E : t \in [0,1] \mapsto \mathbf{\nabla_v}E_t$ is computed using:

$$\mathbf{\nabla_v}E_t = \mathbf{v}_t - K \star \left(\mathrm{Det}\mathrm{J}_{\phi_{t,1}}\nabla I_t^S\left(I_t^S - I_t^T\right)\right), \tag{3}$$

where $\star$ denotes the convolution operator. The velocity field is then updated by computing:

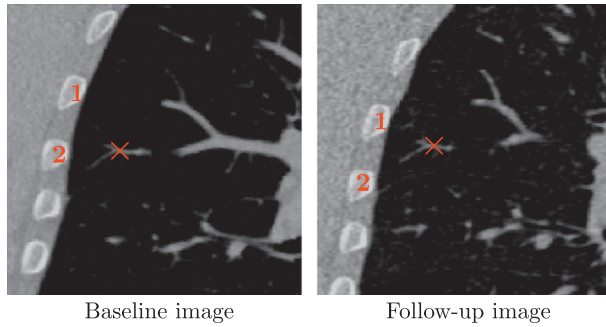$$\mathbf{v} \leftarrow \mathbf{v} - \epsilon\mathbf{\nabla_v}E, \tag{4}$$

Fig. 1. Illustration of the sliding motion at the lung boundary in the coronal view of two CT volumes acquired on the same subject. The motion of the vessel designated by the red cross, and the ribs (1) and (2) clearly demonstrate the sliding motion at the lung boundary. Images out of the EMPIRE10 challenge (Murphy et al., 2011). (For interpretation of the references to colour in this figure legend, the reader is referred to the web version of this article.)

basis to allow the motion of the boundaries at which sliding conditions are modelled. In the diffusion-based method of (Schmidt-Richberg et al., 2012) the displacement field is locally smoothed by distinguishing between the motion normal and tangential to the location of sliding conditions. Though promising, these methods cannot ensure the invertibility of the deformations as they encode the motion within displacement fields, rather than in velocity fields. This is particularly problematic since the magnitude of the pulmonary motion can be very large compared to the deformation magnitude of the surrounding skeletal structures. In this paper, we present a novel approach for modelling sliding conditions in a diffeomorphic framework, which mathematically ensures the estimation of one-to-one mappings.

Diffeomorphic image registration has gained an increasing interest in medical image analysis (Beg et al., 2005; Ashburner, 2007; Avants et al., 2008; Vercauteren et al., 2008; Hernandez et al., 2009; Vialard et al., 2011). These registration algorithms indirectly encode the estimated displacement fields within velocity fields. The deformations between the images are computed by integrating stationary or time-dependent velocity fields in time. In practice, the temporal integration is discretised into Θ time steps. A total displacement field can therefore be seen as the composition of Θ small displacement fields, and its invertibility is ensured if the largest magnitude of the small displacement fields is lower than 0.5 voxels, as exploited first for the Demons algorithm in (Cachier et al., 1999). It is interesting to note that other strategies (Vercauteren et al., 2009; Hermosillo et al., 2002) also rely on the integration of time-varying velocity fields, but these fields are not designed to encode a shortest path according to a given energy, as in (Beg et al., 2005) for instance. A recent discussion of these algorithms has been developed in (Risser et al., 2011). Among them, we consider in this paper the *Large Deformation Diffeomorphic Metric Mapping* (LDDMM) algorithm of (Beg et al., 2005) and the *LogDemons* algorithm of (Vercauteren et al., 2008). These algorithms ensure the invertibility of the deformations and their smoothness. Here, we want to estimate smooth deformations within the structures subject to no sliding motion, and non-smooth deformations at the location of the sliding motion, while preserving the deformations invertibility in the whole domain. This motivates their *piecewise-diffeomorphic* extension.

The paper is organised as follows: We extend the works of (Beg et al., 2005; Vercauteren et al., 2008) to allow sliding motion modelling at region boundaries in Sections 2 and 3, respectively. From a practical point of view, our strategy is based on the use of the heat equation to smooth the velocities in different image regions independently, and a post-treatment of the velocities to ensure the sliding motion. Image regions are fixed in this strategy, although

where ϵ controls the step size during the gradient descent and $\nabla_{\mathbf{v}}E$ is the energy gradient for $t \in [0,1]$. We tune ϵ to be $0.5\max_{x \in \Omega}|\nabla_{\mathbf{v}}E|_{1^{st}\text{ iteration}}^{-1}$, except if $\max_{x \in \Omega}|\epsilon\nabla_{\mathbf{v}}E| > 0.5$, where ϵ is set to $0.5\max_{x \in \Omega}|\nabla_{\mathbf{v}}E|_{\text{current iteration}}^{-1}$. Updates of $\mathbf{v}$ are therefore always below 0.5 voxels and allow for algorithm convergence. Stopping criteria can be a given number of iterations (up to 100 iterations at each resolution in our tests), and/or a maximum value of $|\nabla_{\mathbf{v}}E|$, which is r times lower than at the first iteration ($r = 7.5$ in our tests).

2.2. Piecewise-diffeomorphic registration

2.2.1. Materials

In this subsection, we modify the LDDMM formulation of (Beg et al., 2005) to allow for registration of I_S to I_T with sliding conditions. We subdivide the domain Ω into N subdomains Ω^k, $k \in \{1, \ldots, N\}$ and we denote $\partial\Omega^k$ as the boundaries of Ω^k, as illustrated in Fig. 2a. To model sliding conditions, we develop a mathematical formalism which allows (i) to smooth the velocity field $\mathbf{v}$ in each region Ω^k independently, and (ii) to ensure that the velocity field is parallel to the boundaries $\partial\Omega^k$ for points of Ω^k close to $\partial\Omega^k$. The property (i) obviously prevents exchanges of information between the velocities of different subdomains. As shown in Fig. 2b, it can however lead to the estimation of velocity fields $\mathbf{v}$ compressing some structures against the region boundaries $\partial\Omega^k$. We therefore enforce the deformations to also slide along the boundaries with the property (ii), as illustrated in Fig. 2c.

2.2.2. Admissible Reproducing Kernel Hilbert Space and energy gradients

Instead of considering a Reproducing Kernel Hilbert Space (RKHS) V embedded in $C^1(\Omega, \mathbb{R}^n)$ as in Section 2.1, we utilise here N RKHS of vector fields $V^k \in C^1(\Omega^k, [0,1])$ which can capture sliding motion. Namely the component orthogonal to the boundary vanishes at any point of $\partial\Omega^k$. The set of admissible vector fields is therefore defined by $V := \bigoplus_{k=1}^{N} V^k$, the direct sum of the Hilbert spaces $(V^k)_{k \in [\![1,N]\!]}$. In particular, the norm on V of a vector field $\mathbf{v}_t$ is given by

$$\|\mathbf{v}_t\|_V^2 = \sum_{k=1}^{N} \|\mathbf{v}_t^k\|_{V^k}^2, \tag{5}$$

where $\mathbf{v}_t^k$ is the restriction of $\mathbf{v}_t$ to Ω^k. The flow of any $\mathbf{v} \in L^2([0,1], V)$ is then well defined although the resulting deformations are piecewise-diffeomorphic and not diffeomorphic. As a consequence, the deformation is a diffeomorphism on each subdomain and allows for sliding motion along the boundaries. The registration algorithm is then equivalent to the N independent diffeomorphic registration algorithms of Section 2.1 on each Ω^k.
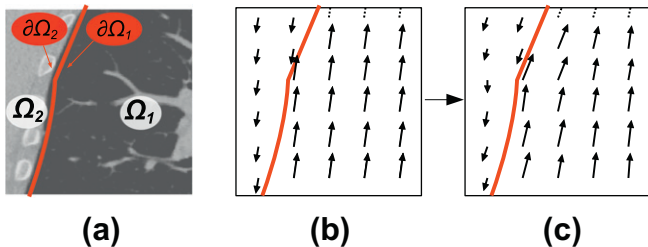

Fig. 2. (a) Subdivision of the registration domain Ω into Ω^1 (inside the lung) and Ω^2. Subdomain boundaries are represented by $\partial\Omega^1$ and $\partial\Omega^2$. (b) Velocity fields $\mathbf{v}$ which can be obtained in Ω after independent smoothing in Ω^1 and in Ω^2, and (c) after enforcing sliding conditions in the neighbourhood of $\partial\Omega^1$ and $\partial\Omega^2$.

2.2.3. Smoothing kernel

We now present a strategy to construct kernels which can capture sliding motion on a domain Ω^k. A computationally efficient approach consists in building a kernel K_ψ^k using (1) a vector mask $\psi^k : x \in \Omega^k \mapsto \psi^k(x) \in L(\mathbb{R}^n)$, where $L(\mathbb{R}^n)$ is the set of linear maps of $\mathbb{R}^n$, which is designed to enforce the sliding constraint along the boundary of Ω^k, and (2) a smoothing kernel K^k which takes into account the geometry of Ω^k:

$$K_\psi^k(x,y) := \psi^k(x)K^k(x,y)[\psi^k(y)]^T. \tag{6}$$

Eq. (6) means that instead of only smoothing a part of the update velocity field $\nabla_{\mathbf{v}}E_t$ with K, as in Eq. (3), we first filter it with ψ^k to enforce the sliding constraint along $\partial\Omega^k$, then smooth it in Ω^k using K^k and finally filter it again with ψ^k. In the end, Eq. (3) is replaced by:

$$\nabla_{\mathbf{v}^k}E_t = \mathbf{v}_t^k - K_\psi^k \star \left(\text{DetJ}_{\phi_{t,1}} \nabla I_t^S \left(I_t^S - I_t^T\right)\right), \quad \forall k \in [\![1, N]\!] \tag{7}$$

where K_ψ^k denotes the kernel associated with the space V^k. The update equation remains Eq. (4).

The constraint on ψ^k is passed by first imposing for any $x \in \partial\Omega^k$, $\langle \psi^k(x)(\mathbf{v}_t(x)), \mathbf{n}(x)\rangle = 0$, where $\mathbf{n}(x)$ is the normal to $\partial\Omega^k$ at x, and $\psi^k(x)(\mathbf{v}_t(x))$ is ψ^k applied to $\mathbf{v}_t(x)$. We use $\psi^k(x) = \mathbf{Id} - \alpha(x)\mathbf{P}_{\mathbf{D}(x)}$, where $\mathbf{P}_{\mathbf{D}(x)}$ is a projection operator to a vector field $\mathbf{D}$ designed to respect this constrain. In order to respect the condition Eq. (2) in Eq. (6), ψ^k must be sufficiently smooth. To do so, $\mathbf{D}(x)$ and $\alpha(x)$ are continuous in Ω^k. Note that a difference with the diffusion-based method of (Schmidt-Richberg et al., 2012) is that we do not allow any exchange of information between the different regions Ω^k.

Now the key point is to design the kernel K^k. A Gaussian kernel may be not satisfactory since it does not take into account the intrinsic geometry of the domain Ω^k. In practice, smoothing a velocity field $\mathbf{w}$ in a region Ω^k with a Gaussian kernel would transform $\mathbf{w}$ inside Ω^k, which is what we want, but also outside of Ω^k, which is undesired. To take the intrinsic geometry into account, we propose to use the kernel defined by the heat equation on Ω^k with Neumann boundary conditions, as explained in Appendix A. The fact that the heat kernel satisfies the condition Eq. (2) can be found in (Grigor'yan, 2009). Diffusing $\mathbf{w}$ with the heat equation during a time $\tau \in [0, \Gamma]$ and in an infinite domain is equivalent to smoothing $\mathbf{w}$ with a Gaussian kernel of standard deviation $\sqrt{2\Gamma}$ (Weierstrass transform). Our smoothing therefore differs from a standard Gaussian convolution only in the neighbourhood of $\partial\Omega^k$, where no information is shared with the voxels outside of Ω^k. In what follows, we therefore refer to kernels K^k equivalent to Gaussian kernels of standard deviation σ by smoothing $\mathbf{w}$ in Ω^k with the heat equation during $\tau \in [0, \sigma^2/2]$. Algorithmic details of our strategy are given hereafter.

2.2.4. Piecewise-diffeomorphic registration algorithm

Having decided on the smoothing kernel, we subdivide the domain Ω into N subdomains Ω^k. We consider the vector field $\mathbf{D}$ so that for each point $x \in \Omega$, $x + \mathbf{D}(x)$ is the nearest boundary between two subdomains. This field is constructed only once, prior to the image registration. We also build $\mathbf{D}$ in a limited neighbourhood around the boundaries $\partial\Omega^k$, in practice for $\|\mathbf{D}(x)\|_{L^2} < \gamma$. For the registration of pulmonary images, we empirically use values of γ of about 20 mm. Consider a velocity field $\mathbf{w}$ defined on Ω. We use $\mathbf{D}$ to enforce the sliding conditions around $\partial\Omega^k$ by reducing the contributions of $\mathbf{w}(x)$ in the direction of $\mathbf{D}(x)$, when $\|\mathbf{D}(x)\|_{L^2} < \gamma$:

$$\mathbf{w}(x) = \mathbf{w}(x) - \alpha(x)\mathbf{D}(x)\frac{<\mathbf{w}(x), \mathbf{D}(x)>_{L^2}}{\|\mathbf{D}(x)\|_{L^2}^2}, \tag{8}$$

where the weight $\alpha(x)$ equals $(\gamma - \|\mathbf{D}(x)\|)^2/\gamma$. For numerical stability, $\mathbf{w}(x)$ is set to 0 if $\|\mathbf{D}(x)\|_{L^2}^2 = 0$. We emphasise that γ must be small compared to the spatial extent of Ω^k (about 300 millimetres width for the thoracic cage). In particular, defining $\mathbf{D}$ at equal distance to two opposite boundaries of Ω^k can lead to discontinuous deformations. Neighbouring voxels of $\mathbf{D}$ indeed point to locations of $\partial\Omega^k$ in opposite directions there, so $\mathbf{D}$ is discontinuous. Registration algorithm on Ω^k is:

The time-dependent velocity field $\mathbf{v}^k$ is initialised to 0
repeat
  for $\theta = 1 \to \Theta$ **do**
    {*Compute the deformations at time t_θ*}
    Compute ϕ_{t_θ}, ϕ_{1,t_θ}, $\phi_{t_\theta,1}$, $I^S_{t_\theta}$ and $I^T_{t_\theta}$ as explained in
  Section 2.1
    {*Compute and smooth the gradient of*} E_{t_θ}
    $\mathbf{u}_{t_\theta} \leftarrow \left(\mathrm{DetJ}_{\phi_{t,1}} \nabla I^S_{t_\theta} \left(I^S_{t_\theta} - I^T_{t_\theta} \right) \right)$
    Treat u_{t_θ} using Eq. (8)
    $\mathbf{u}_{t_\theta} \leftarrow K^k \star \mathbf{u}_{t_\theta}$ using the heat equation, as explained in
  Appendix A
    Treat $\mathbf{u}_{t_\theta}$ using Eq. (8)
    $\nabla_{\mathbf{v}^k} E_{t_\theta} \leftarrow \mathbf{v}^k_{t_\theta} - \mathbf{u}_{t_\theta}$
  end for
  {*Update $\mathbf{v}^k$*}
  for $\theta = 1 \to \Theta$ **do**
    $\mathbf{v}^k_{t_\theta} \leftarrow \mathbf{v}^k_{t_\theta} - \epsilon \nabla_{\mathbf{v}^k} E_{t_\theta}$
  end for
until Convergence

In this algorithm, the step {*Compute and smooth the gradient of* $\mathbf{v}$} replaces Eq. (3) in the standard LDDMM algorithm, the step {*Update $\mathbf{v}^k$*} is equivalent to Eq. (4), and the t_θ, $\theta \in [1, \cdots, \Theta]$ are the time steps which discretise the time interval $[0, 1]$.

3. Piecewise-diffeomorphic LogDemons registration

3.1. Overview of the Log-Domain Diffeomorphic Demons

In this subsection, we give an overview of the LogDemons framework of (Vercauteren et al., 2008). Similarly to the previous Section 2, we consider a source image I_S registered on a target image I_T in the domain Ω. The image I_S is transformed through the time-dependent diffeomorphic transformation $\phi^\mathbf{v}_t$, $t \in [0, 1]$ which is defined by a stationary velocity field $\mathbf{v}$ in the domain Ω, and not a time-dependent one like in (Beg et al., 2005), using: $\frac{\partial}{\partial t}\phi^\mathbf{v}_t = \mathbf{v}(\phi^\mathbf{v}_t)$, where $\phi^\mathbf{v}_0 = \mathbf{Id}$. The final deformation is called the exponential map of $\mathbf{v}$, $\exp(\mathbf{v}) \doteq \phi^\mathbf{v}_1$. The optimal velocity field $\tilde{\mathbf{v}}$ is obtained by computing $\tilde{\mathbf{v}} = \arg\ \min_\mathbf{v} E(\mathbf{v}, \mathbf{v}_c)$, where the energy E is defined as:

$$E(\mathbf{v}, \mathbf{v}_c) = \frac{1}{\lambda_i^2} \left\| I_T - I_S \circ (\phi^{\mathbf{v}_c}_1)^{-1} \right\|^2_{L^2} + \frac{1}{\lambda_x^2} \left\| \log\left(\phi^\mathbf{v}_1 \circ (\phi^{\mathbf{v}_c}_1)^{-1}\right) \right\|^2_{L^2}$$
$$+ \frac{1}{\lambda_d^2} \|\nabla\mathbf{v}\|^2_{L^2}, \tag{9}$$

where the logarithm log is the inverse operation of the exponential and the velocity field $\mathbf{v}_c$ encodes an intermediate transformation $\phi^{\mathbf{v}_c}_1$, called correspondence. In Eq. (9), the first term measures the SSD between the registered images, the second term measures the correspondence between the smooth deformation $\phi^\mathbf{v}_1$ and the deformation $\phi^{\mathbf{v}_c}_1$, and the third term measures the spatial regularity of $\mathbf{v}$. Insights about the influence of the parameters λ_i, λ_x, λ_d are

thoroughly developed in (Mansi et al., 2011). Minimisation of E $(\mathbf{v}, \mathbf{v}_c)$ is as follows:

The stationary velocity field $\mathbf{v}$ is initialised to 0
repeat
  {*Compute the deformation*}
  Compute $\phi^\mathbf{v}_1$ using $\phi^\mathbf{v}_0 = \mathbf{Id}$ and $\frac{\partial}{\partial t}\phi^\mathbf{v}_t = \mathbf{v}(\phi^\mathbf{v}_t)$
  {*Compute and smooth the update field $\delta\mathbf{v}$*}
  $\delta\mathbf{v} \leftarrow - \left[(I_T - I_S \circ (\phi^\mathbf{v}_1)^{-1}) / \left(\|\mathbf{G}\|^2 + \lambda_i^2/\lambda_x^2 \right) \right] \mathbf{G}$
  $\delta\mathbf{v} \leftarrow K_{fluid} \star \delta\mathbf{v}$ (fluid-like regularisation)
  {*Update and smooth the velocity field $\mathbf{v}$*}
  $\mathbf{v}_c \leftarrow \mathbf{v} + \delta\mathbf{v} + [\mathbf{v}, \delta\mathbf{v}]/2$ (BCH approximation)
  $\mathbf{v} \leftarrow K_{diff} \star \mathbf{v}_c$ (diffusion-like regularisation)
until Convergence

In this algorithm $\mathbf{G}(x) = \nabla(I_S \circ (\phi^\mathbf{v}_1)^{-1})(x)$, $\forall x \in \Omega$. The Baker–Campbell–Hausdorff (BCH) approximation is also an estimate of $\mathbf{v}_c = \log(\phi^\mathbf{v}_1 \circ \phi^{\delta\mathbf{v}}_1)$. More details are given in (Vercauteren et al., 2008).

3.2. Piecewise-diffeomorphic extension

Inspired by the piecewise-diffeomorphic extension of the LDDMM algorithm (Beg et al., 2005) presented in the previous section, we now propose a piecewise-diffeomorphic extension of the LogDemons algorithm of (Vercauteren et al., 2008) in this subsection. As in Section 2.2.4, we subdivide the domain Ω into N subdomains Ω^k and we consider a vector field $\mathbf{D}$ so that for each point $x \in \Omega$, $x + \mathbf{D}(x)$ is the nearest boundary between two subdomains. Instead of smoothing $\delta\mathbf{v}$ and $\mathbf{v}_c$ homogeneously in space, we smooth them in each region Ω^k independently. We also enforce the velocities $\mathbf{v}(x)$ and $\mathbf{v}_c(x)$ to be parallel to the boundaries $\partial\Omega^k$ for points x close to $\partial\Omega^k$. We denote K^k_{fluid} and K^k_{diff} the smoothing kernels to perform fluid and diffusion regularisation in Ω^k using the technique of A. We then minimise $E(\mathbf{v}, \mathbf{v}_c)$ as follows:

The stationary velocity field $\mathbf{v}$ is initialised to 0
repeat
{*Compute the deformation*}
Compute $\phi^\mathbf{v}_1$ using $\phi^\mathbf{v}_0 = \mathbf{Id}$ and $\frac{\partial}{\partial t}\phi^\mathbf{v}_t = \mathbf{v}(\phi^\mathbf{v}_t)$
{*Compute and smooth the update field $\delta\mathbf{v}$*}
$\delta\mathbf{v} \leftarrow - \left[(I_T - I_S \circ (\phi^\mathbf{v}_1)^{-1}) / \left(\|\mathbf{G}\|^2 + \lambda_i^2/\lambda_x^2 \right) \right] \mathbf{G}$
$\delta\mathbf{v} \leftarrow K^k_{fluid} \star \delta\mathbf{v}$ in each region Ω^k using the heat equation, as
  explained in Appendix A
{*Update and smooth $\mathbf{v}$*}
$\mathbf{v}_c \leftarrow \mathbf{v} + \delta\mathbf{v} + [\mathbf{v}, \delta\mathbf{v}]/2$ (BCH approximation)
Treat $\mathbf{v}_c$ using Eq. (8)
Ω^k : $\mathbf{v} \leftarrow K^k_{diff} \star \mathbf{v}_c$ in each region Ω^k using the heat equation,
  as explained in Appendix A
Treat $\mathbf{v}$ using Eq. (8)
until Convergence

---

4. Piecewise-diffeomorphic registration of the lungs

The driving application of this work is the estimation of the pulmonary motion in which the lung boundaries slip along the thoracic cage (also known as the rib cage) boundary, the thoracic cage boundary moves very smoothly, and the motion of the structures inside and outside of the thoracic cage is relatively smooth. Our piecewise-diffeomorphic extensions of (Beg et al., 2005 and

Vercauteren et al., 2008), presented in Sections 2.2 and 3.2 allow to capture the sliding motion between different regions, but do not allow the motion of the region boundaries. We consequently subdivide the diffeomorphic registration problem into two steps, plus an optional third one:

1. After computing the rigid alignment R between the images, we compute a diffeomorphism $\tilde{\phi}$ which estimates the motion of the thoracic cage boundaries with a large amount of regularisation. We do not model any sliding condition here. The large amount of regularisation is justified by the fact that the motion of the thoracic cage boundary tends to be very smooth during the respiratory cycle.
2. We split the domain Ω, containing $I_S \circ R^{-1} \circ \tilde{\phi}_1^{-1}$, into Ω^T and $\Omega^R \doteq \Omega - \Omega^T$, where Ω^T contains the thoracic cage. We note $\partial\Omega^R$ and $\partial\Omega^T$ the subdomain boundaries. By using a piecewise-diffeomorphic strategy of Section 2 or 3, we then estimate the diffeomorphism $\hat{\phi}$ which independently registers the structures in Ω^T and Ω^R with a sliding motion at $\partial\Omega^T/\partial\Omega^R$.
3. We can also estimate a diffeomorphism $\bar{\phi}$ which improves the registration accuracy at a fine scale in Ω. No sliding condition is modelled here.

The registration scheme is summarised in Fig. 3. Piecewise-diffeomorphic strategies are only used in step (2) and any standard diffeomorphic registration algorithm can be used in steps (1) and (3). Note that step (3) is motivated by practical reasons. Smoothing the deformations using the heat equation and Neumann boundary conditions is slower than by convolving them homogeneously in space, typically using Fast Fourier Transforms. To keep the computational burden reasonable, we can therefore perform step (2) on undersampled images and step (3) on images at full resolution. It is worth mentioning that step (1) can also be reasonably performed on undersampled images, although not necessary, due the large amount of regularisation.

5. Evaluation

In this section, we evaluate the proposed piecewise-diffeomorphic strategy on 2D and 3D image pairs. We summarise here the notations used in this section:

- *Registration framework*: Registration using (**LDM**) the LDDMM framework (Beg et al., 2005), or (**LogD**) the LogDemons framework (Vercauteren et al., 2008).
- *Regularisation strategy*: Regularisation using (**Kσ**) a Gaussian kernel of standard deviation σ, or (**MK**) a kernel constructed as the sum of several Gaussian kernels (Risser et al., 2011), or (**MR**) a multi-resolution strategy with decreasing registered images smoothing and decreasing deformation regularisation for increasing image resolution. (**S-.**) Regularisation using sliding motion modelling.
- *Registration quality*: (**O(ρ)**) Overlap (or Dice coefficient) of a region ρ in two registered images I_1 and I_2. Its value is defined as [#voxels $\in (\rho_1 \cap \rho_2)$]/ [#voxels $\in (\rho_1 \cup \rho_2)$], so 0 means no

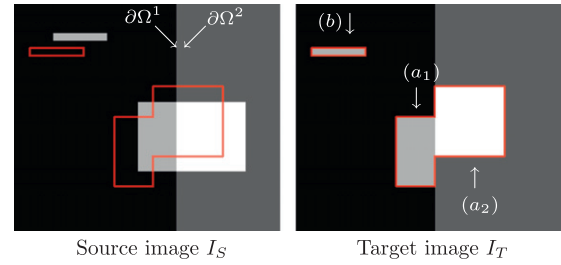Source image I_S Target image I_T

Fig. 4. Synthetic 2D images I_S and I_T registered in Section 5.1. We consider the shapes (a_1), (a_2) and (b) in the images. Their boundaries in I_T are represented by the red outline. The domain Ω is subdivided into Ω^1 (black background) and Ω^2 (dark grey background). (For interpretation of the references to colour in this figure legend, the reader is referred to the web version of this article.)

overlap and 1 means an accurate overlap. (**DetJ**) Determinant of the Jacobian. On a given domain, the lower its maximum (M (DetJ)), the smoother the sharpest deformation. Negative DetJ (DetJ < 0) also indicate the points where the deformation is not invertible. (**SSD**) Sum of squared difference between two registered images.

5.1. Results on synthetic 2D data

In this subsection, we evaluate our piecewise-diffeomorphic strategies on the synthetic 2D images I_S and I_T presented in Fig. 4. The domain Ω of the source image I_S is subdivided into two subdomains Ω^1 (black background) and Ω^2 (dark grey background). The boundary between Ω^1 and Ω^2 moves to the left from I_S to I_T. Homogeneous motion down and up is also observed in Ω^1 and in Ω^2, respectively. This breaks the main shape (a) lying on Ω^1 and Ω^2 into (a_1) and (a_2). This also generates a displacement of the long thin shape (b) of Ω^1.

We first registered I_S and I_T using standard LDDMM registration (Beg et al., 2005) with Gaussian smoothing kernels of standard deviation σ of 1, 3, 9 and 30 pixels (LDM K1–30), plus a multi-scale smoothing kernel of (Risser et al., 2011) with 10 characteristic scales ranging from 1 to 30 pixels (LDM MK). We also performed multi-resolution LogDemons registration, with decreasing image smoothing and deformation regularisation for increasing image resolution (LogD MR). We finally composed the deformations obtained using (LDM K30) with LDDMM registration using σ = 30 pixels and sliding motion modelling (S-LDM K30) and with multi-resolution LogDemons using sliding motion modelling (S-LogD MR). Note that for LDDMM registration a multi-resolution scheme would have no impact on the estimated deformations, as explained in (Risser et al., 2011). Results are illustrated in Fig. 5 and quantified in Table 1.

We can first remark that none of the LDDMM strategies without sliding motion modelling gives satisfactory results. When the amount of smoothing is low, the thin shape (b) is not translated because of the absence of overlap between its locations in I_S and in I_T. Transporting (b) can be addressed using a large amount of regularisation here. In this case, the motion down of (a_1) in Ω^1 can indeed
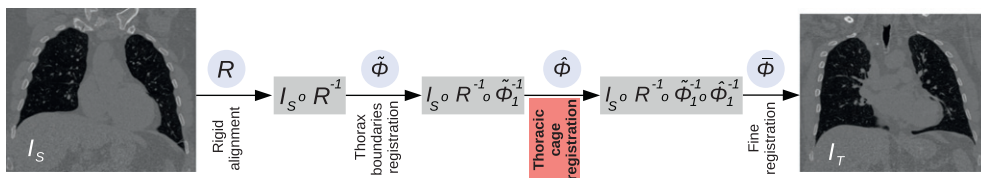

Fig. 3. Registration of the 3D pulmonary images I_S (source/ moving) and I_T (target/fixed) after rigid alignment R (which maps I_S image space into I_T image space): (1) thoracic cage boundaries are registered through $\tilde{\phi}$; (2) the structures within the thoracic cage are then registered through $\hat{\phi}$; (3) fine diffeomorphic registration $\bar{\phi}$ is finally performed. The estimation of the diffeomorphism $\hat{\phi}$ requires sliding motion modelling and the estimation of $\bar{\phi}$ and $\bar{\phi}$ only requires standard diffeomorphic registration.
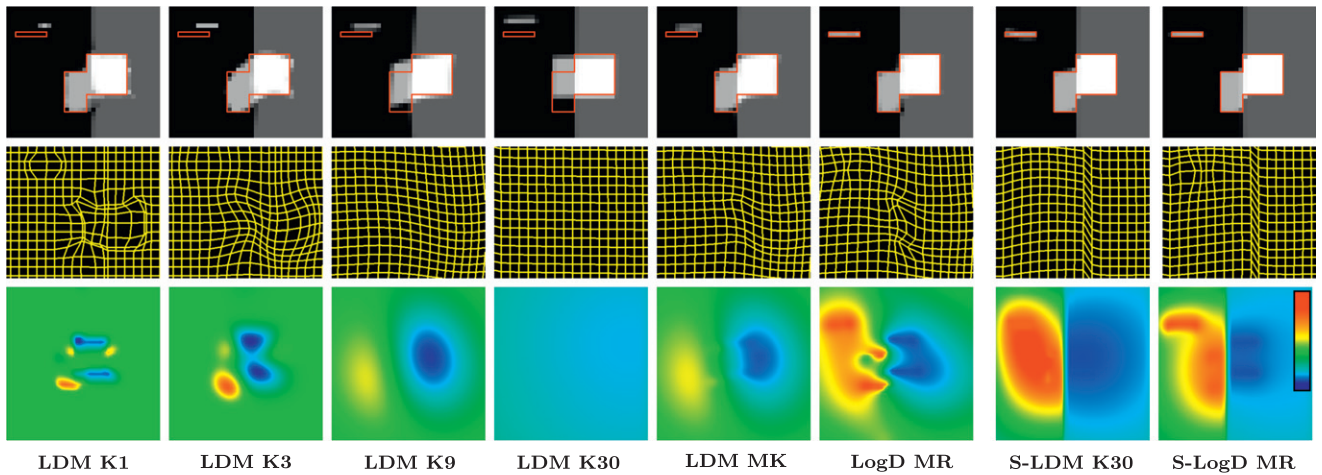
LDM K1   LDM K3   LDM K9   LDM K30   LDM MK   LogD MR   S-LDM K30   S-LogD MR

Fig. 5. Registration of the synthetic images I_S and I_T of Fig. 4 using **(LDM)** LDDMM or **(LogD)** LogDemon with different options: **(Kσ)** smoothing a Gaussian kernel of standard deviation σ, **(MK)** multi-kernel smoothing of (Risser et al., 2011), **(MR)** multi-resolution strategy with smoothed images at a coarse resolution and **(S-)** sliding motion modelling between the subdomains Ω^1 and Ω^2 presented in Fig. 4. **(Top)** Deformed source images. Shape boundaries in the target image I_T are represented by the red outline. **(Centre)** Deformed grids. **(Bottom)** Deformation magnitude on the y-axis (top/bottom). Scale bar ranges from -2.2 to 2.2 pixels. (For interpretation of the references to colour in this figure legend, the reader is referred to the web version of this article.)

Table 1
Quantitative results obtained when registering the synthetic images I_S and I_T of Fig. 4 using the options of Fig. 5. **(O(ρ))** is the overlap (or Dice coefficient) of the region ρ between the registered images and **(M(DetJ))** is the maximum Jacobian determinants in $\Omega - \partial\Omega^1$.

	LDM K1	LDM K3	LDM K30	LDM MK	LogD MR	S-LDM K30	S-LogD MR
O (a_1)	0.71	0.68	0.60	0.72	0.96	0.98	0.98
O (a_2)	0.85	0.83	0.85	0.92	1	0.98	0.98
O (b)	0	0	0	0	1	1	1
M (DetJ)	4.08	1.96	1.12	1.28	2.13	1.16	1.20

make move (b). However, as observed in (LDM K9), (LDM K30) and (LDM MK) the motion up of (a_2) in Ω^2 does not allow to capture its motion down in Ω^1 without sliding conditions. As shown by the results on (S-LDM K30), a smooth motion and an accurate matching are finally obtained using sliding motion modelling. The transport of (b) can also be addressed without sliding motion modelling using a multi-resolution strategy, like in (LogD MR). However, as shown in the deformed grids and deformations on the y-axis of Fig. 5, more homogeneous deformations are clearly observed when sliding conditions are explicitly modelled. This observation, which can be considered as more natural, is confirmed by the simultaneous low M (DetJ) and high region overlaps observed using sliding conditions. Finally, we can remark that we obtained similarly satisfactory results using (S-LDM K30) and (S-LogD MR).

5.2. Results on synthetic 3D data

We now evaluate our sliding motion modelling strategy with LDDMM and LogDemons registration on 3D phantom images. We generated the 3D phantom images of the thorax using the 4D NURBS-based Cardiac-Torso (NCAT phantom) toolkit (Segars, 2001), as presented in Fig. 6. This toolkit is a realistic and flexible simulation tool for generating CT volumes and modelling cardiac and respiratory motion. Here, the images have a size of $192 \times 192 \times 192$ voxels and a resolution of 2 mm. They represent different levels of the respiratory cycle, from the end of expiration (I_1) to the end of inhalation (I_5) with intermediate states (I_2, I_3 and I_4).

We registered I_1 on I_2, I_3, I_4 and I_5 to evaluate the benefit of our sliding motion strategy on 3D images presenting different magnitudes of sliding motion. To do so, we followed the strategy of
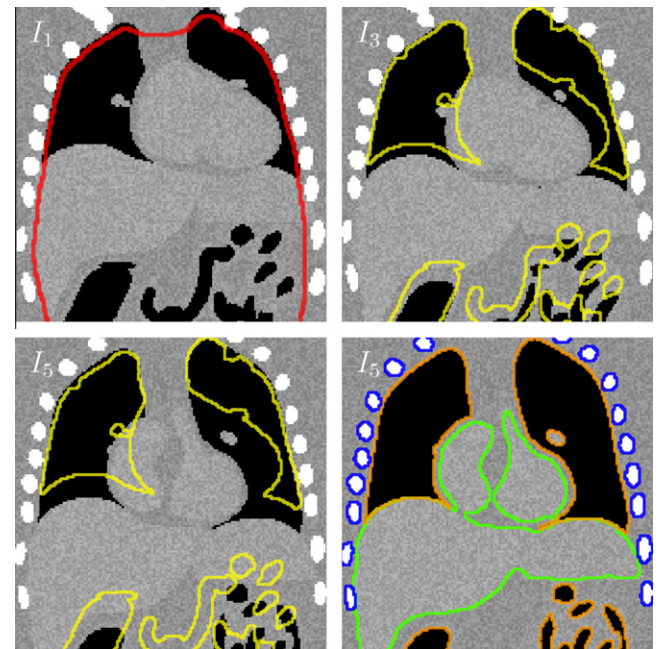

Fig. 6. 3D NCAT images of Section 5.2 at end of expiration (I_1), intermediate state (I_3) and end of inhalation (I_5). In I_1, the red outline indicates where the sliding conditions are modelled. In I_3 and I_5 (bottom-left), the yellow outline represents the boundary of the lungs and intestines in I_1. In I_5 (bottom-right), the segmented structures used for the overlaps are shown: bones are emphasised by the blue outlines, lungs and intestines by the orange outlines and light grey soft tissues by the green outline. (For interpretation of the references to colour in this figure legend, the reader is referred to the web version of this article.)

Section 4 with and without sliding motion modelling: (i) We first aligned the segmented ribs and spine using LogDemons registration. This step corresponds to the estimation of $\tilde{\phi}$ in Fig. 3. We only performed fluid regularisation with a Gaussian kernel K_{fluid} having a standard deviation of 100 mm. (ii) We then performed a finer registration of the image structures using similar strategies as in the previous subsection: Multi-resolution LogDemons (LogD MR), piecewise-diffeomorphic LogDemons (S-LogD), and piecewise-diffeomorphic LDDMM (S-LDM). We tuned the smoothing parameters to obtain deformations having similar levels of smoothness for each strategy. This step corresponds to the estimation of $\hat{\phi}$ in Fig. 3. Computations were performed at half resolution here. Note that the thoracic cage of I_0 was segmented using template registration. (iii) We finally improved the image matching using multi-resolution LogDemons. This last step corresponds to the estimation of $\bar{\phi}$ in Fig. 3. In what follows, we compare the final deformations $\tilde{\phi}_1^{-1} \circ \hat{\phi}_1^{-1} \circ \bar{\phi}_1^{-1}$ obtained using the different strategies of step (ii). Results are illustrated in Fig. 7. Overlap of different structures, presented at the bottom-right of Fig. 6 are given in Fig. 8.

As shown by the results of Fig. 8, the larger the sliding motion the more pertinent our strategy. The overlaps are indeed similar for (LogD MR), (S-LogD) and (S-LDM) when I_1 is registered to I_2 and I_3. The overlaps are however clearly higher for (S-LogD) and (S-LDM) than for (LogD MR), when registering I_1 to I_4 and I_5. This is explained by the fact that the general motion down of the thoracic cage (in green in Fig. 7) is propagated outside of the cage by the regularisation when no sliding conditions are modelled. The larger this motion compared to the motion of the structures outside of the cage, the lower the ability of the algorithm to capture accurate deformations in the whole domain Ω. Similarly to what we observed in Section 5.1, discontinuous LogDemons and LDDMM also lead to equivalent satisfactory results. This is particularly true as all methods led to similar deformation smoothness: The maximum difference between the M (DetJ) outside of the location of sliding conditions was found when registering I_1 to I_5, with M (DetJ) equals 1.84 and 3.2 for (LogD MR) and (S-LDM), respectively. We consider that these values are relatively similar as the

maximum Jacobian of 3D deformations is compared. No negative DetJ was also found in all deformations, thoracic cage boundary included. It is worth mentioning that (S-LogD) was about 5 times faster than (S-LDM) and required about seven times less memory. This is mainly due to the fact that the LDDMM framework uses time-dependent velocity fields ($\Theta = 10$ time-steps here) whereas the LogDemons framework uses stationary velocity fields. In summary, modelling sliding conditions explicitly improved the registration of images that exhibit a non-negligible sliding motion. Moreover, the piecewise-diffeomorphic strategy (S-LogD) estimated similar deformations as (S-LDM), but with lower computational resources.

5.3. Results on the EMPIRE10 dataset

In this subsection, we show the benefit of the proposed piecewise-diffeomorphic LogDemons strategy on real 3D pulmonary CT images from the EMPIRE10 challenge (Murphy et al., 2011).[1] This challenge provides 30 lung image pairs to register and uses a detailed protocol to evaluate the registration quantitatively as well as qualitatively. We denote (I_S^n, I_T^n), $n = \{1, \ldots, 30\}$ the 30 source (moving) and target (fixed) images. Interestingly, different image pairs of the challenge require capturing various amplitudes of sliding motion. We estimated this amplitude, in the coronal slice where the rib cage has the largest width, as the distance between the points of (I_S^n, I_T^n) at the left or right intersection between the inferior part of the lungs and the rib cage boundary. We divided the image data into three groups according to this amplitude: (Group G1) Image pairs presenting little sliding motion, from 1 to 12 mm. It contains subjects 2, 3, 4, 5, 6, 9, 12, 13, 15, 19, 26 and 29. (Group G2) Image pairs presenting a moderate amount of sliding motion, from 13 to 33 mm. It contains subjects 8, 10, 11, 16, 17, 22, 23, 24, 25, 27, 30. (Group G3) Image pairs presenting a large amount of sliding motion, from 48 to 80 mm. It contains subjects 1, 7, 14, 18, 20, 21, 28.

Note that most images have resolutions of about one cubic millimetre. Exemplar cases from all three groups are illustrated in Fig. 9.

To compare the pipeline of Section 4 with other techniques, we first performed a series of tests on the image pair 17 of the EMPIRE10 challenge. This image pair corresponds to two images of the POPI model (Vandemeulebroucke et al., 2007). The sliding motion observed in this subject has an amplitude of about 14 mm. We registered $\left(I_S^{17}, I_T^{17}\right)$ using the pipeline of Section 4 with sliding motion modelling, as well as using the strategy of (Delmon et al., 2011), and using multi-resolution LogDemons registration (Vercauteren et al., 2008) of the masked lungs. Results are discussed in Section 5.3.2.

We also performed a second series of tests, on all 30 image pairs, to compare the pipeline of Section 4 with and without sliding motion modelling. Results are discussed in Section 5.3.3. Note that they are not compared to those of (Murphy et al., 2011) for two reasons: (1) As explained in Section 1, we cannot affinely register the lung masks and then non-rigidly register the images, strategy adopted by most successful methods in (Murphy et al., 2011). (2) The sliding motion is not covered by the EMPIRE10 challenge evaluation criteria.

5.3.1. Pre-processing and parameter selection

We worked on the original (uncropped) images of the EMPIRE10 challenge having a large size of up to $512 \times 512 \times 500$ voxels. As discussed in the previous subsection, piecewise-diffeomorphic LDDMM registration requires heavy computational resources for large 3D images, while having a similar ability as
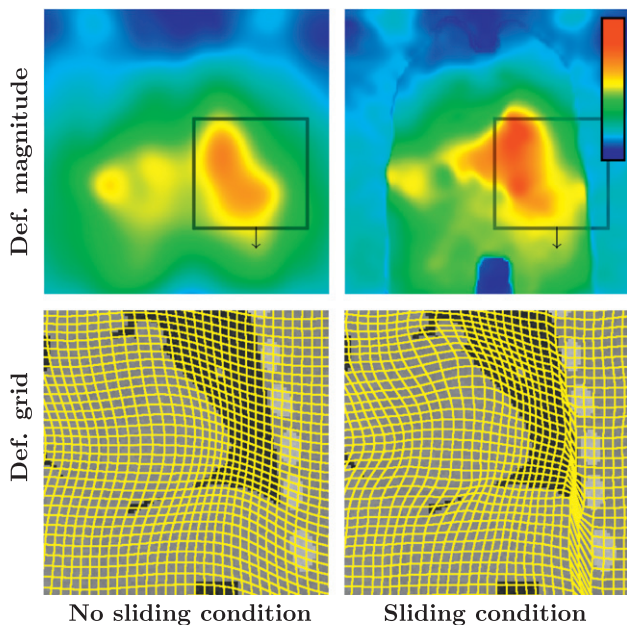

Fig. 7. Deformation magnitude and deformed grids obtained when registering I_1 to I_5 using LogDemons using sliding motion modelling (S-LogD) or not (LogD MR). Colour bar is from 0 to 5 cm. (For interpretation of the references to colour in this figure legend, the reader is referred to the web version of this article.)

Def. magnitude

Def. grid

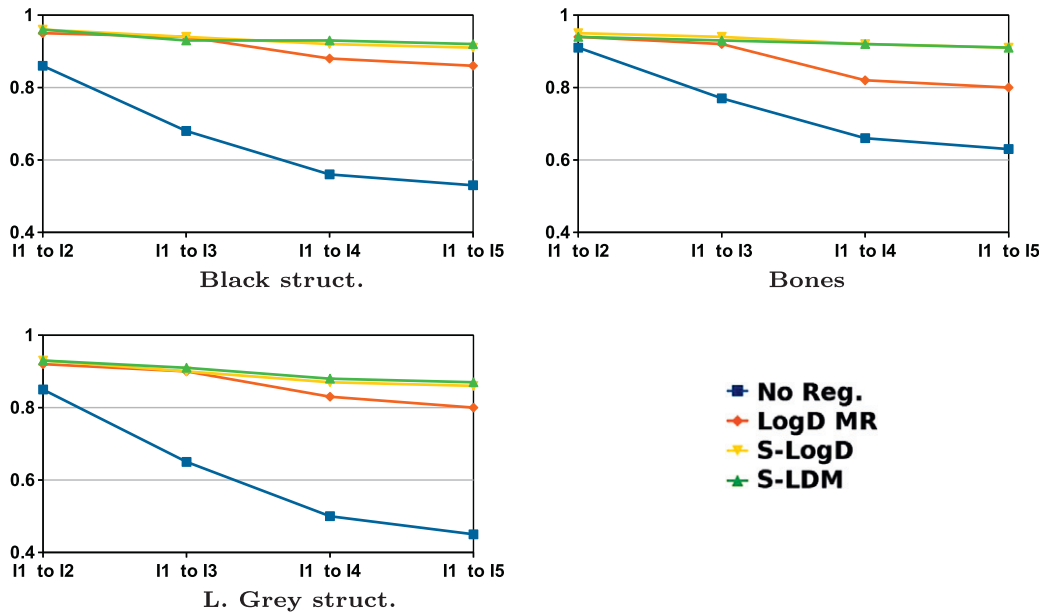No sliding condition   Sliding condition

Fig. 8. Overlap between the registered lungs and intestines (Black struct.), the light grey soft tissues (L. Grey struct.) and the bones (Bones) after registering I_1 to I_2, I_3, I_4 and I_5.
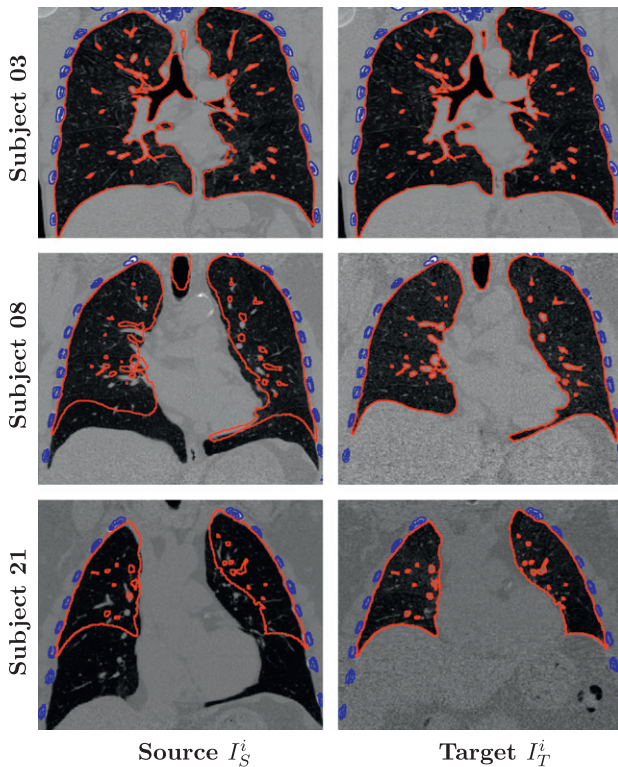

Fig. 9. 3D CT images out of the 30 subjects of the EMPIRE10 challenge (Murphy et al., 2011). Subject 03 does not present any sliding motion (group G1), subject 08 presents a fairly large amount of sliding motion (group G2), and subject 21 presents a very large amount of sliding motion (group G3). The lung and rib boundaries are represented by the red and blue outlines, respectively. (For interpretation of the references to colour in this figure legend, the reader is referred to the web version of this article.)

Table 2
Quantitative results of Section 5.3.2, obtained on subject 17 of the EMPIRE10 challenge (Murphy et al., 2011). Registered images correspond to two time frames of the POPI model (Vandemeulebroucke et al., 2007). (**SSD**) is the normalised sum of squared difference between the registered images in the whole domain Ω. (**lmk. comp.**) is the average distance between 41 landmarks defined in the lungs. Corresponding standard deviations are between parentheses. (%**DetJ** < 0) is the percentage of negative determinant of Jacobians (DetJ) in the whole domain Ω. (**M(DetJ**)) is the maximum DetJ in the whole domain, except at the thorax boundary $(\Omega - \partial\Omega^1)$.

	SSD	lmk. comp.	%DetJ < 0	M (DetJ)
No Reg.	1.000	5.74 (2.77)	N/A	N/A
S-FFD	0.855	1.36 (0.607)	0.219	5.88
S-LogD	0.756	1.54 (0.697)	0	2.70
Msk-LogD	1.001	1.56 (0.787)	0	2.74

piecewise-diffeomorphic LogDemons registration to capture a sliding motion between two images. In this subsection, we therefore only used the pipeline of Section 4 with LogDemons based methods. This pipeline was used as follow:(i) Each diffeomorphism $\hat{\phi}^n$, capturing the thoracic cage motion, was estimated using LogDemons registration with fluid-like regularisation only and a Gaussian kernel K_{fluid} having a standard deviation of 100 mm. Images were subsampled by a factor 3. We estimated each $\hat{\phi}^n$ by registering the segmented spines and the ribs of I_S^n and I_T^n. Their segmentation was first performed using simple thresholding followed by morphological operations. Segmentation could be improved using advanced segmentation techniques, e.g. (Ramakrishnan et al., 2011). However, we applied a large amount of spatial regularisation, as the sought deformations are very smooth, and found a fairly coarse bone segmentation to be sufficient. (ii) We estimated the general motion $\hat{\phi}^n$ inside and outside of the thoracic cage using multi-resolution LogDemons with (S-LogD MR) and without (LogD MR) sliding motion modelling. At the coarsest scale, the images were registered using fluid and diffusion regularisations with Gaussian kernels having standard deviations of 30 and 5 mm, respectively. At the finest scale, corresponding kernels had standard deviations of 15 and 1 mm, respectively. Note that for (S-LogD MR) the heat equation was used with parameters making it equivalent to Gaussian kernels with sliding motion modelling, as explained in Section 2.2.3. Images were subsampled by a factor 3. (iii) Estimation of the final diffeomorphisms $\hat{\phi}^n$, which capture fine deformations, was performed at full resolution using multi-resolution LogDemons (Vercauteren et al., 2008). We used a similar multi-resolution approach as in Sections 5.1 and 5.2. Note that instead of registering the original images, we treated them using
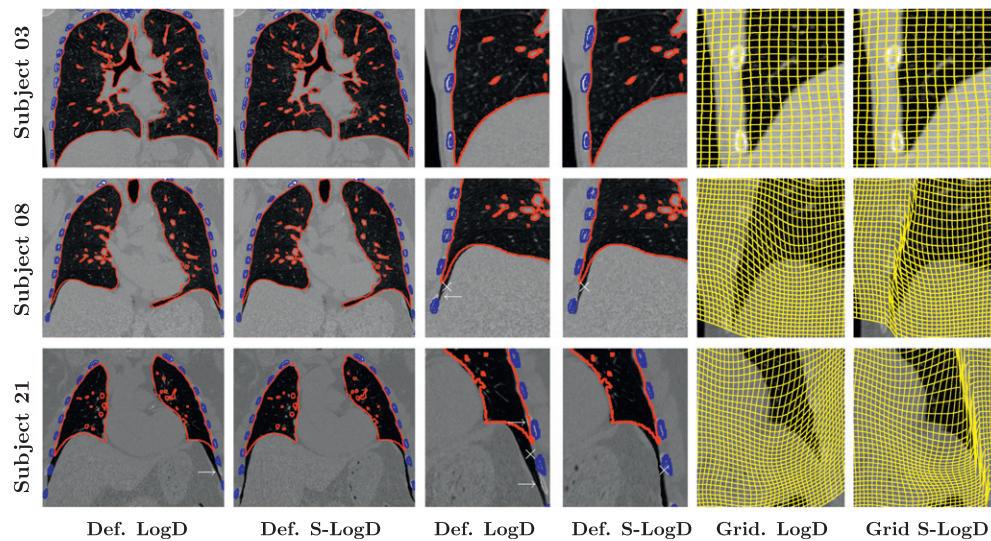
Fig. 10. Qualitative results obtained when registering the 3D CT images presented in Fig. 9. Subjects 03, 08 and 21 are representative of the groups G1, G2 and G3 respectively. Deformed source images without and with sliding conditions are presented in (**Def.LogD**) and (**Def. S-LogD**). White arrows emphasise ribs which are not accurately registered. White crosses show black bands on the deformed images at the thoracic cage boundary. Corresponding grids in a region of interest are shown in (**Grid LogD**) and (**Grid S-LogD**).

anisotropic diffusion (Perona and Malik, 1990) and contrast enhancement in the lungs. Contrast enhancement was performed by multiplying the grey levels of I_S^n and I_T^n by 5 in the lungs.

For the registration algorithm of (Delmon et al., 2011), we used the freely available implementation of Elastix (Klein et al., 2010).[2] This algorithm is a non-diffeomorphic Free-Form Deformation algorithm with sliding conditions modelling, so we use (**S-FFD**) to refer to it. The registration parameters we used are those of (Delmon et al., 2011) and can be found on Elastix' website.[3]

The last registration strategy we used is inspired from the method A of (Murphy et al., 2011): In contrast to all other registration experiments in this paper, we performed an affine alignment of the masked images, instead of a rigid alignment of the segmented ribs and spine. The lungs were also masked when performing non-rigid deformation. Multi-resolution LogDemons (Vercauteren et al., 2008) registration was performed with the same resolutions and smoothing parameters as those for the pipeline of Section 4. We use (**Msk-LogD**) to refer to the results. Note that the method A of (Murphy et al., 2011) uses diffeomorphic demons registration (Vercauteren et al., 2009) rather than LogDemons registration.

5.3.2. Results on subject 17 (POPI model)

Quantitative measures of the registration quality obtained using (S-FFD), (S-LogD) and (Msk-LogD) are given in Table 2. For comparison purposes corresponding measures obtained before registration are also given (No Reg.) Best matching quality was clearly reached for the methods modelling sliding motion (S-FFD) and (S-LogD). This is first measured by the SSD in the whole domain Ω which is clearly higher for (S-FFD) and (S-LogD) than for (Msk-LogD). The reason is obvious as the deformation of (Msk-LogD) was computed using the information contained in the lungs only. Landmarks comparison was also performed using 41 landmarks identified in the lungs by medical experts and freely available on POPI model's website.[4] Distances between the registered landmarks are given in mm in the column (lmk. comp.) of Table 2. Here, equivalent results are obtained for (S-FFD), (S-LogD) and (Msk-LogD) with

Table 3
Quantitative results obtained when registering the 30 image pairs of the EMPIRE10 challenge (Murphy et al., 2011). Results are averaged for the subjects requiring little sliding motion (**G1**), those requiring a fairly large amount of sliding motion (**G2**), and those requiring a large amount of sliding motion (**G3**). Corresponding standard deviation are shown between parentheses. (**M(DetJ)**) is the maximum determinant of the Jacobians (DetJ) in the whole domain, except at the thorax boundary. (**SSD lng**) is the sum of squared difference between the registered images in the lungs. (**O(Ribs)**) is the overlap of the segmented ribs between the registered images. Ribs segmentation was relatively coarse, so low overlaps do not necessarily mean non-accurate matchings.

		G1	G2	G3
M (DetJ)	S-LogD	2.85 (0.96)	3.56 (1.63)	7.23 (1.77)
	LogD	2.75 (0.88)	3.19 (1.40)	7.06 (1.56)
SSD lng	S-LogD	0.373 (0.074)	0.454 (0.133)	0.800 (0.081)
	LogD	0.376 (0.069)	0.457 (0.130)	0.825 (0.090)
O (Ribs)	S-LogD	0.765 (0.047)	0.762 (0.045)	0.760 (0.046)
	LogD	0.761 (0.049)	0.750 (0.042)	0.680 (0.052)

slightly lower distances for (S-FFD). This can be explained by the fact that smoother deformations were estimated for (S-LogD) and (Msk-LogD) than for (S-FFD), as emphasised by their lower M (DetJ). Finally, the key result here is that no negative DetJ was obtained using the diffeomorphic techniques (S-LogD) and (Msk-LogD) but DetJ down to -6.59 were found for (S-FFD) at the thoracic cage boundary. Only deformations obtained using a diffeomorphic framework therefore allowed to ensure a one-to-one mapping between the registered images here.

5.3.3. Results on all 30 subjects

Registration of the images of Fig. 9 is illustrated in Fig. 10. Quantitative results, averaged in the groups G1, G2 and G3 are given in Table 3. In the deformed grids of Fig. 10, one can observe that for case 03, which presents very little motion, the sliding conditions have no apparent impact on the registration result. However, for cases 08 and 23 of groups G2 and G3 respectively, sliding conditions allow to capture the sliding motion visibly. This is further emphasised by the white arrows showing ribs which were only satisfactorily registered using sliding conditions. We can however see that although the matching of the pulmonary vessels is accurate for cases 03 and 08, it is inaccurate for case 21, with or without

---

[2] http://elastix.isi.uu.nl/.
[3] 'par0016' in the parameter file database of Elastix's wiki.
[4] http://www.creatis.insa-lyon.fr/rio/popi-model/.

sliding conditions. We can also observe a black band on the deformed images between the thoracic cage boundary and the structures below the lungs, as shown by the white crosses. For (LogD), this band is due to the deformations regularisation. For (S-LogD), it is due to the trilinear interpolation when upsampling the velocity field **v**, as explained in Section 6. Deformed grids show that the impact of this phenomenon is spatially limited using (S-LogD), compared to what is observed using (LogD).

These observations can be discussed in more depth with the results of Table 3. By comparing the average M (DetJ) for (LogD) and (S-LogD), we can first remark that similar deformation smoothness was obtained with or without sliding conditions for G1, G2 and G3. It is interesting to note that the larger the amount of observed sliding motion, the larger the benefit of sliding conditions modelling for the pulmonary vessels and ribs matching accuracy. This is measured by SSD of the registered structures within the lungs and the ribs overlap. In G1, the SSD and the overlaps are very similar in average for (LogD) and for (S-LogD). In G2, they are slightly better for (S-LogD) than for (LogD). In G3, they are clearly better for (S-LogD) than for (LogD). These results are consistent with those obtained on synthetic data in Section 5.2. Note that we also measured lung overlaps, which were always similar using (S-LogD) or (LogD). We can also remark that the average SSD in the lungs is clearly higher for G3 than for G1 and G2. The matching of the pulmonary vessels is therefore not as accurate in G3 than in G1 and G2, as already observed in Fig. 10. For the subjects of G3 some negative DetJ were also observed for (S-LogD) at the thoracic cage boundary $\partial\Omega^1$, where the sliding motion is modelled. This is due to an insufficient temporal discretisation when integrating the velocity fields **v** to compute the deformations ϕ_1^v. Lowest DetJ of -8.9 was found for subject 21 with 0.09% of voxels having negative DetJ. This however is still low given the fact that differences of more than 60 mm are found on the z-axis between neighbouring voxels of **v** for this subject. As a comparison, 1.13% voxels have negative DetJ using the non-diffeomorphic technique (S-FFD) on subject 21, and the lowest DetJ is -43.3. No other negative DetJ was found using (S-LogD) in G1 and G2, as well as outside of $\partial\Omega^1$ for G3. Note finally that for subjects 01, 20 and 21, which require very large deformations, we locally estimated artifactual discontinuous mappings in the trachea, at the top of the thoracic cage.

We can conclude from these results that modelling sliding conditions improves the matching of the ribs and pulmonary vessels, whatever the amount of observed sliding motion. This benefit is however not sufficient in subjects requiring a very large amount of sliding motion to obtain satisfactory pulmonary vessel matchings. Modelling sliding conditions everywhere at the thoracic cage boundary can also lead to local artifactual discontinuities in subjects requiring a very large amount of sliding motion. Addressing these two issues is for future work, as will be discussed in Section 6.

6. Discussion

Our results demonstrate that the proposed piecewise-diffeomorphic LDDMM (S-LDM) and LogDemons (S-LogD) strategies allow to capture sliding motion in 3D CT lung images, by regularising the deformations in different image subdomains independently. We mentioned in Section 5.2 that the key advantage of (S-LogD), in the context of this paper, is its use of a stationary velocity field to encode the deformations of lower computational complexity, in contrast to the time-dependent velocity field of (S-LDM) which has much higher memory requirements. Other numerical aspects of the piecewise-diffeomorphic LogDemons algorithm make it particularly attractive in the context of the registration of thoracic images with sliding motion. For example, stationary velocity fields can first be integrated in time using the fast

scaling-and-squaring algorithm described in (Arsigny et al., 2006) while time-dependent ones require standard incremental techniques, such as Euler or Leap frog scheme. In our experiments, we therefore integrated 128 times steps using $\log_2(128) = 7$ displacement field compositions for (S-LogD), which was faster than the 10 compositions required for (S-LDM) with 10 time steps.

Another subtle numerical benefit of using the LogDemons formalism when modelling discontinuities is the following: it does not only regularise the update velocity fields (fluid regularisation), like in the LDDMM formalism, but also the velocity fields themselves (diffusion regularisation). Since the diffusion regularisation is performed iteration after iteration on the same velocity field, it can turn out to be less pronounced than the fluid regularisation for a similar level of regularisation. As shown in Appendix A, we perform region-wide smoothing in each Ω^i by solving the heat equation using a finite differences scheme (fractional-steps). In this scheme, for a given time step, the higher the amount of iterations, the higher the regularisation. A large amount of regularisation therefore requires more computational time than a small amount of regularisation. As a result, using diffusion regularisation requires less computational resources than fluid regularisation for a similar smoothness level. To counterbalance these remarks, first recall that only our piecewise-diffeomorphic LDDMM algorithm is fully founded from a mathematical point of view. In general, the LDDMM formalism can also encode the deformations in initial momenta, which can be very interesting for some applications, e.g. (Vaillant et al., 2004; Singh et al., 2010). However, we do not use this property in the present paper.

An issue also arose in Section 5.3, when using different resolutions at steps (2) and (3) of our registration pipeline. These steps were respectively performed with a subsampling factor 3 and at full resolution. Trilinear interpolation was also performed to upsample the velocity field **v** obtained at step (2). As a result, **v** was locally smoothed at the thoracic cage boundary, so a black band appeared there. This issue was not solved at step (3) because it is designed to estimate smooth deformations in the whole image domain. This phenomenon is however not very penalizing as it only affects the registration quality in a limited neighbourhood around the discontinuities.

Finally, we emphasise that our strategy requires accurate segmentations of the thoracic cage. For instance, a non-accurate segmentation, which labels a bone as being two subdomains, is likely to lead to an unrealistic mapping. As discussed in the next section, developing accurate thoracic cage segmentation techniques is one of the main outlooks of this work.

7. Conclusion

We have presented a novel piecewise-diffeomorphic registration method which successfully addresses the problem of sliding motion modelling. The proposed formalism in which the deformations are embedded in stationary or time-dependent velocity fields allows to model large deformations with locally abrupt discontinuities, while mathematically preserving the invertibility of the deformations. Importantly, using sliding conditions instead of a homogeneous regularisation gave us the opportunity to recover more realistic respiratory motion, not only inside but also outside of the lungs. This is particularly true in regions where the images present few clear features and some knowledge is required to regularise the deformations realistically. The piecewise-diffeomorphic LDDMM formalism developed in this paper is mathematically founded and was shown to be able to register 3D CT lung images requiring large deformations and sliding motion. We have also proposed to incorporate the main ideas of the piecewise-diffeomorphic LDDMM formalism into the LogDemons diffeomorphic

registration framework (Vercauteren et al., 2008). As shown by our results, in Section 5, this piecewise-diffeomorphic LogDemons extension is particularly interesting when registering large 3D images as it has a similar ability as the piecewise-diffeomorphic LDDMM algorithm to capture sliding motion, but is computationally more efficient.

We expect that the presented work will open new research directions from a theoretical, application and technical point of view:

- (*Theoretical*) Presently, the location of boundaries at which the sliding motion is modelled is fixed. To recover the respiratory motion, we therefore compensated the thoracic cage boundaries motion before independently registering the regions inside and outside the thoracic cage, as presented in Section 4. Theoretical developments could be introduced to simultaneously estimate the motion of the structures within each region, as well as the motion of the region boundaries, as in (Delmon et al., 2011; Schmidt-Richberg et al., 2012). Other similarity measures than the sum of squared difference could also be of interest.
- (*Application*) Registration of the whole thorax, as opposed to the lung masks only, will be helpful for radiotherapy planning and delivery. It is obvious that modelling more finely the registered images would help to estimate even more realistic *whole body* deformations. There is for instance a sliding motion between the lungs and the liver, and another one between the lungs and the heart that we have not modelled. Some parts of the thoracic cage boundary also do not present any sliding motion, as discussed in Section 5.3. We used a model which can improve the motion estimation around the thoracic cage compared to a model without any sliding condition. The motion estimation could however be even more realistic using additional information about the sliding condition location. This would however require finer segmentations of the thoracic cage.
- (*Technical*) As explained in Appendix A, the applied smoothing scheme to capture sliding conditions is based on region-wide smoothing. Finer sliding conditions would probably involve to model the discontinuities on surfaces with holes (*e.g.* at the thoracic cage boundary but not in the trachea). They could otherwise involve the definition of *anchors* (*e.g.* the trachea) to locally prevent the estimation of sliding motion. More advanced smoothing strategies would then be required. Working on fine techniques to up-sample discontinuous velocity fields would also help to reduce the computational burden.

In the future, we finally plan to apply the piecewise-diffeomorphic registration technique to other organs and structures that exhibit locally discontinuous motion patterns.

Appendix A. Region-wide smoothing

We consider here a velocity field $\mathbf{v}$ diffused using the heat equation $\partial \mathbf{v}/\partial \tau = \Delta \mathbf{v}$ in a region Ω^k during a *virtual* time $\tau \in [0, \Gamma]$. We also consider Neumann conditions at the region boundaries: $\nabla \mathbf{v}(x) \cdot \mathbf{n} = 0$ for $x \in \partial \Omega^k$, where $\mathbf{n}$ is the normal to $\partial \Omega^k$ at point x. Here, Γ controls the amount of smoothing. We use a finite difference approach to smooth $\mathbf{v}$ in Ω^k only:

1. We consider a temporary vector field $\mathbf{v}' \in \Omega$ that we fill with $\mathbf{v}' = \mathbf{v}$ in Ω^k and with $\mathbf{0}$ otherwise.
2. We propagate around Ω^k the values of $\mathbf{v}'$ which are at the inner region boundary $\partial \Omega^k$. The propagation is performed in a margin of typically 4 voxels. The use of this propagation is to generate *mirror* data around $\partial \Omega^k$ which simulate the Neumann conditions.
3. The values of $\mathbf{v}'$ are diffused using the heat equation with Neumann boundary conditions. Using an explicit scheme would be extremely limiting here due to a Courant–Friedrichs–Lewy (CFL) condition which would require the use of very small time steps to preserve the algorithm stability. A straightforward implicit scheme would also be extremely slow as we diffuse 3D images. Huge diagonal-by-block matrices should be inverted. We therefore use the fractional-steps scheme explained page 141 in (Tannehill et al., 1997). At each iteration, this scheme sequentially diffuses the image in the *x*, *y* and *z* direction using a 1D implicit scheme. It therefore only requires the inversion of tri-diagonal matrices, which can be efficiently addressed using the Thomas algorithm of (Press et al., 1992). In addition it is unconditionally stable, which allows the use of fairly large time steps.
4. We finally copy the smoothed values of $\mathbf{v}'$ into $\mathbf{v}$ on the domain Ω^k only.

References

Arsigny, V., Commowick, O., Ayache, N., Pennec, X., 2009. A fast and log-euclidean polyaffine framework for locally linear registration. Journal of Mathematical Imaging and Vision 33, 222–238.

Arsigny, V., Commowick, O., Pennec, X., Ayache, N., 2006. A log-Euclidean framework for statistics on diffeomorphisms, in: International Conference on Medical Image Computing and Computer Assisted Intervention (MICCAI) – LNCS, pp. 924–931.

Ashburner, J., 2007. A fast diffeomorphic image registration algorithm. NeuroImage 38, 95–113.

Avants, B.B., Epstein, C.L., Grossman, M., Gee, J.C., 2008. Symmetric diffeomorphic image registration with cross-correlation: evaluating automated labeling of elderly and neurodegenerative brain. Medical Image Analysis 12, 26–41.

Beg, F.M., Miller, M.I., Trouvé, A., Younes, L., 2005. Computing large deformation metric mappings via geodesic flows of diffeomorphisms. International Journal of Computer Vision 61, 139–157.

Bruveris, M., Risser, L., Vialard, F.X., 2012. Mixture of kernels and iterated semi-direct product of diffeomorphism groups. SIAM Multiscale Modeling and Simulation 10, 1344–1368.

Cachier, P., Pennec, X., Ayache, N., 1999. Fast Non-Rigid Matching by Gradient Descent: Study and Improvements of the Demons Algorithm. Technical Report RR-3706. INRIA.

Coselmon, M.M., Balter, J.M., McShan, D.L., Kessler, M.L., 2004. Mutual information based CT registration of the lung at exhale and inhale breathing states using thin-plate splines. Medical Physics 31, 2942–2948.

Delmon, V., Rit, S., Pinho, R., Sarrut, D., 2011. Direction dependent b-splines decomposition for the registration of sliding objects. In: Proceedings of the MICCAI Workshop on Pulmonary Image Analysis, pp. 45–55.

Grigor'yan, A., 2009. Heat Kernel and Analysis on Manifolds. AMS/IP Studies in Advanced Mathematics.

Hermosillo, G., Chefd'hotel, C., Faugeras, O., 2002. Variational methods for multimodal image matching. International Journal of Computer Vision 50, 329–343.

Hernandez, M., Bossa, M.N., Olmos, S., 2009. Registration of anatomical images using paths of diffeomorphisms parameterized with stationary vector field flows. International Journal of Computer Vision 85, 291–306.

Klein, S., Staring, M., Murphy, K., Viergever, M.A., Pluim, J.P.W., 2010. elastix: a toolbox for intensity based medical image registration. IEEE Transactions on Medical Imaging 29, 196–205.

Li, B., Christensen, G.E., Hoffman, E.A., McLennan, G., Reinhardt, J.M., 2003. Establishing a normative atlas of the human lung: intersubject warping and registration of volumetric CT images. Academic Radiology 10, 255–265.

Mansi, T., Pennec, X., Sermesant, M., Delingette, H., Ayache, N., 2011. iLogDemons: a demons-based registration algorithm for tracking incompressible elastic biological tissues. International Journal of Computer Vision 92, 92–111.

Mattes, D., Haynor, D., Vesselle, H., Lewellen, T., Eubank, W., 2003. PET-CT image registration in the chest using free-form deformations. IEEE Transactions on Medical Imaging 22, 120–128.

McClelland, J.R., Blackall, J.M., Tarte, S., Chandler, A.C., Hughes, S., Ahmad, S., Landau, D.B., Hawkes, D.J., 2006. A continuous 4D motion model from multiple respiratory cycles for use in lung radiotherapy. Medical Physics 33, 3348–3358.

Murphy, K., Van Ginneken, B., Reinhardt, J.M., Kabus, S., Ding, K., Deng, X., Pluim, J.P.W., et al., 2011. Evaluation of registration methods on thoracic CT: the EMPIRE10 challenge. IEEE Transactions on Medical Imaging 30, 1901–1920.

Pace, D.F., Enquobahrie, A., Yang, H., Aylward, S.R., Niethammer, M., 2011. Deformable image registration of sliding organs using anisotropic diffusive regularization. In: 2011 IEEE International Symposium on Biomedical Imaging: From Nano to Macro, pp. 407–413.

Perona, P., Malik, J., 1990. Scale-space and edge detection using anisotropic diffusion. IEEE Transactions on Pattern Analysis and Machine Intelligence 12, 629–639.

Press, W.H., Teukolsky, S.A., Vetterling, W.T., Flannery, B.P., 1992. Numerical Recipes in C the Art of Scientific Computing. second ed.. Cambridge University Press.

Ramakrishnan, S., Alvino, Christopher, Grady, L., Kiraly, A., 2011. Automatic three-dimensional rib centerline extraction from CT scans for enhanced visualization and anatomical context. In: Proceedings of Information Processing in Medical Images, pp. 79622X–79622X-12.

Risser, L., Vialard, F.X., Wolz, R., Murgasova, M., Holm, D.D., Rueckert, D., 2011. Simultaneous multiscale registration using large deformation diffeomorphic metric mapping. IEEE Transactions on Medical Imaging 30, 1746–1759.

Ruan, D., Esedoglu, S., Fessler, J., 2009. Discriminative sliding preserving regularization in medical image registration. In: Proceedings of IEEE International Symposium on Biomedical Imaging (ISBI), pp. 430–433.

Schmidt-Richberg, A., Werner, R., Handels, H., Ehrhardt, J., 2012. Estimation of slipping organ motion by registration with direction-dependent regularization. Medical Image Analysis 16, 150–159.

Segars, W.P., 2001. Development of a new dynamic NURBS-based cardiac-torso (NCAT) phantom. Ph.D. thesis, The University of North Carolina.

Singh, N., Fletcher, P.T., Preston, J.S., Ha, L., King, R., Marron, J.S., Wiener, M., Joshi, S., 2010. Multivariate statistical analysis of deformation momenta relating anatomical shape to neuropsychological measures. In: International Conference on Medical Image Computing and Computer Assisted Intervention (MICCAI) – LNCS, pp. 529–537.

Sluimer, I., Schilham, A., Prokop, M., van Ginneken, B., 2006. Computer analysis of computed tomography scans of the lung: a survey. IEEE Transactions on Medical Imaging 25, 385–405.

Sommer, S., Lauze, F., Nielsen, M., Pennec, X., 2011a. Kernel bundle EPDiff: evolution equations for multi-scale diffeomorphic image registration. In: Scale Space and Variational Methods in Computer Vision, pp. 677–688.

Sommer, S., Nielsen, M., Lauze, F., Pennec, X., 2011b. A multi-scale kernel bundle for LDDMM: towards sparse deformation description across space and scales. In: Proceedings of Information Processing in Medical Images, pp. 624–635.

Stewart, C.V., Lee, Y.L., Tsai, C.L., 2004. An uncertainty-driven hybrid of intensity-based and feature-based registration with application to retinal and lung CT images. In: International Conference on Medical Image Computing and Computer Assisted Intervention (MICCAI) – LNCS, pp. 870–877.

Tannehill, J., Anderson, D., Pletcher, R., 1997. Computational Fluid Mechanics and Heat Transfer. second ed.. Taylor & Francis.

Vaillant, M., Miller, M.I., Trouvé, A., Younes, L., 2004. Statistics on diffeomorphisms via tangent space representations. NeuroImage 23, S161–S169.

Vandemeulebroucke, J., Bernard, O., Rit, S., Kybic, J., Clarysse, P., Sarrut, D., 2012. Automated segmentation of a motion mask to preserve sliding motion in deformable registration of thoracic CT. Medical Physics 39, 1006–1015.

Vandemeulebroucke, J., Sarrut, D., Clarysse, P., 2007. The POPI-model, a point-validated pixel-based breathing thorax model. In: International Conference on the Use of Computers in Radiation Therapy (ICCR), p. 6247.

Vercauteren, T., Pennec, X., Perchant, A., Ayache, N., 2008. Symmetric log-domain diffeomorphic registration: a demons-based approach. In: International Conference on Medical Image Computing and Computer Assisted Intervention (MICCAI) – LNCS, pp. 754–761.

Vercauteren, T., Pennec, X., Perchant, A., Ayache, N., 2009. Diffeomorphic demons: efficient non-parametric image registration. NeuroImage 45, S61–S72.

Vialard, F.X., Risser, L., Rueckert, D., Cotter, C.J., 2011. Diffeomorphic 3D Image Registration via Geodesic Shooting using an Efficient Adjoint Calculation. International Journal of Computer Vision.

Werner, R., Ehrhardt, J., Schmidt, R., Handels, H., 2009. Patient-specific finite element modeling of respiratory lung motion using 4D CT image data. Medical Physics 36, 1500–1511.

Werner, R., Ehrhardt, J., Schmidt-Richberg, A., Heiß, A., Handels, H., 2010. Estimation of motion fields by non-linear registration for local lung motion analysis in 4D CT image data. International Journal of Computer Assisted Radiology and Surgery 5, 595–605.

Wu, Z., Rietzel, E., Boldea, V., Sarrut, D., Sharp, G.C., 2008. Evaluation of deformable registration of patient lung 4DCT with subanatomical region segmentations. Medical Physics 35, 775–781.

Yin, Y., Hoffman, E., Lin, C.L., 2010. Lung lobar slippage assessed with the aid of image registration. In: International Conference on Medical Image Computing and Computer Assisted Intervention (MICCAI) – LNCS, pp. 578–585.